Experimental study of the NaK 3 $^3\Pi$ double minimum state

L. Morgus, P. Burns, R. D. Miles, A. D. Wilkins, U. Ogba,[a)]
A. P. Hickman, and J. Huennekens
Department of Physics, Lehigh University, Bethlehem, Pennsylvania 18015

(Received 13 January 2005; accepted 28 January 2005; published online 11 April 2005)

We have used the Doppler-free, perturbation-facilitated optical-optical double-resonance technique to investigate the vibrational, rotational, and hyperfine structure of the 3 $^3\Pi$ double minimum state of NaK. Since this electronic state arises from an avoided crossing with the nearby 4 $^3\Pi$ state, we observe striking patterns in the data that provide a sensitive probe of the electronic wave function in the various regions of the double well potential. A single-mode cw dye laser excites $2(A)\ ^1\Sigma^+(v_A,J)\sim 1(b)\ ^3\Pi_{\Omega=0}(v_b,J)$ mixed singlet-triplet "window" levels from thermally populated rovibrational ground state levels, $1(X)\ ^1\Sigma^+(v_X,J\pm 1)$. Further excitation by a single-mode cw Ti:sapphire laser selects various $3\ ^3\Pi_0(v_\Pi,J_\Pi)$ rovibrational levels, which are detected by observing direct $3\ ^3\Pi_0\rightarrow 1(a)\ ^3\Sigma^+$ fluorescence in the green spectral region. Using the inverse perturbation approximation method, we have determined a 3 $^3\Pi_0$ potential curve that reproduces the measured energies to $\sim 0.24\ \mathrm{cm}^{-1}$. In addition, the hyperfine and spin–orbit constants, b_F and A_v, have been determined for each region of the potential curve. © *2005 American Institute of Physics*.
[DOI: 10.1063/1.1875132]

I. INTRODUCTION

The perturbation-facilitated optical-optical double-resonance (PFOODR) technique has proven to be a powerful mechanism for studying high lying triplet electronic states of alkali diatomic molecules. Since the electronic ground state of all neutral alkali molecules is a spin singlet ($S=0$), the dipole selection rule on spin, $\Delta S=0$, prohibits direct excitation of excited triplet states. However, spin–orbit perturbations couple specific rovibrational levels of the $b\ ^3\Pi$ and the $A\ ^1\Sigma^+$ states, creating mixed singlet/triplet "window" levels that allow access to higher lying triplet states. With the use of narrow-band continuous-wave (cw) lasers, the PFOODR method is inherently Doppler-free, leading to very high resolution excitation spectra. Previous experiments using this method have focused primarily on the homonuclear diatomic molecules, Li_2,[1–10] Na_2,[8,11–21] and K_2,[22–25] and to a lesser extent on the heteronuclear molecules NaK (Refs. 26 and 27) and $^6Li^7Li$.[28,29]

In the present work, we employ this technique to study the 3 $^3\Pi$ double minimum state of NaK, which was first observed in vibrational wave packet spectroscopy, but without rovibrational level resolution, by Berg *et al.*[30] Later, Hansson carried out a detailed study of the collisionally populated NaK 3 $^3\Pi$ state (obtaining the value $T_e=24\ 630\ \mathrm{cm}^{-1}$) following one-color two-photon excitation of the 3 $^1\Pi$ state.[31] Excitation of NaK molecules to several different electronic states results in strong green $3\ ^3\Pi\rightarrow 1(a)\ ^3\Sigma^+$ fluorescence.[26,30,31] Therefore, it seems that collisional processes tend to funnel population into the NaK 3 $^3\Pi$ state, similar to the situation with the $2\ ^3\Pi_g$ state of the homonuclear alkali molecules. The latter is responsible for the ubiquitous Na_2 violet and K_2 yellow bands.[32–38]

The hyperfine structure of the NaK $2(c)\ ^3\Sigma^+$, $1\ ^3\Delta$, $4\ ^3\Sigma^+$, and $1(b)\ ^3\Pi$ electronic states has been measured, and the Fermi contact constants for all these states are found to be within a few percent of the value $1.0\times 10^{-2}\ \mathrm{cm}^{-1}$.[26,27,39–43] This similarity is due to the fact that these are all Rydberg states dominated by the ion-core ground state configuration. The double minimum exhibited by the 3 $^3\Pi$ electronic state of NaK results from an avoided curve crossing with the nearby 4 $^3\Pi$ state. Since the 3 $^3\Pi$ adiabatic state has contributions from several diabatic states, the vibrational, rotational, fine, and hyperfine splittings are expected to be quite different in different regions of the potential. The 3 $^3\Pi$ and 4 $^3\Pi$ states also present an interesting opportunity to study nonadiabatic couplings.

In the present work, a total of 290 $3\ ^3\Pi_{\Omega=0}(v,J)$ levels with $6\leqslant v\leqslant 53$ were excited from 16 sets of $2(A)\ ^1\Sigma^+\sim 1(b)\ ^3\Pi_{\Omega=0}$ window levels. The inverted perturbation approximation (IPA) method[44] was then used to construct a potential curve from the observed energy level positions. A few levels of the 3 $^3\Pi_{\Omega=2}$ state were also measured using two new $2(A)\ ^1\Sigma^+\sim 1(b)\ ^3\Pi_{\Omega=2}$ window levels. The energy separations between rovibrational level $\Omega=0$ and $\Omega=2$ fine structure components were used to determine the NaK 3 $^3\Pi$ spin–orbit interaction constant A_v as a function of vibrational quantum number. These values, along with the hyperfine splittings of the 3 $^3\Pi_{\Omega=0}$ level energies, were in turn used to obtain the Fermi contact constant b_F as a function of v.

This paper is organized as follows. Section II provides a brief description of the experimental setup, while Sec. III discusses the rotational level structure and the method used to establish the absolute vibrational numbering of the 3 $^3\Pi$ state. The mapping of the 3 $^3\Pi$ state potential using the IPA

[a)]Present address: Benedict College, 1600 Harden Street, Columbia, South Carolina 29204.

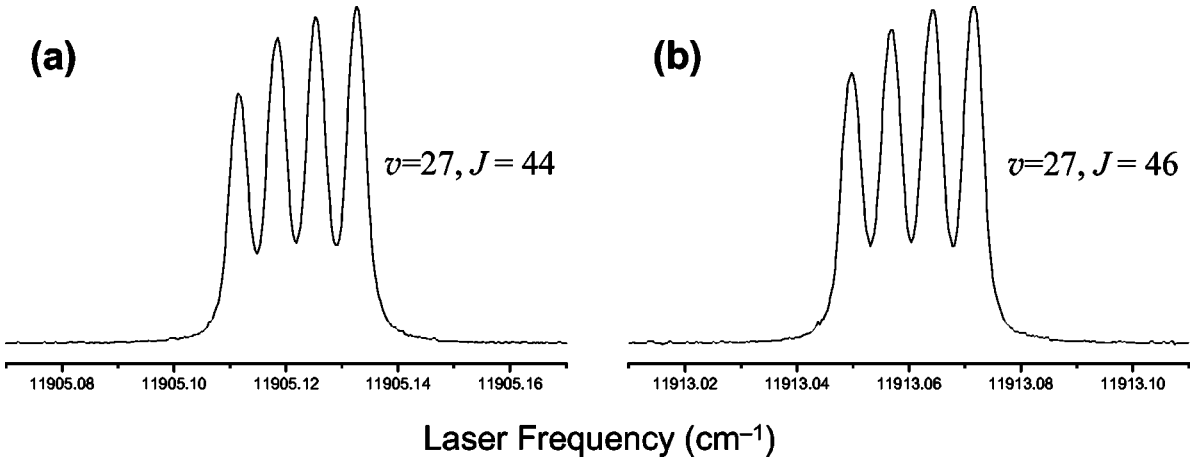

FIG. 1. Excitation line shapes for (a) the NaK $3\,^3\Pi_0(v=27,J=44) \leftarrow 1(b)\,^3\Pi_0(v=18,J=45)$ transition (P_{11} line) and (b) the $3\,^3\Pi_0(v=27,J=46) \leftarrow 1(b)\,^3\Pi_0(v=18,J=45)$ transition (R_{11} line).

method is described in Sec. IV. Section V discusses the interesting region just below the barrier where primarily inner well levels, primarily outer well levels, and mixed levels coexist. Experimental and simulated bound-free $3\,^3\Pi_0(v,J) \rightarrow 1(a)\,^3\Sigma^+$ fluorescence spectra are presented in Sec. VI, and an analysis of the $3\,^3\Pi_0$ state fine and hyperfine structure is provided in Sec. VII. A few concluding remarks can be found in Sec. VIII.

II. EXPERIMENT

The experimental setup has been described previously in Ref. 26 and is shown in Fig. 1 of that reference. Briefly, a sodium-potassium mixture is contained in a stainless steel, cross-shaped heat-pipe oven that is heated to $T \sim 365-395\,^\circ$C to vaporize the metal. Argon buffer gas (pressure $\sim 0.5-1.8$ Torr) is used to keep the alkali metal away from the windows.

A Coherent model 699-29 single-mode cw dye laser produces $\sim 140-470$ mW of power in the $730-775$ nm range using LD700 dye. This laser (the pump laser) is used to excite NaK molecules from a level $1(X)\,^1\Sigma^+(v_X,J\pm1)$ of the electronic ground state to a particular mixed singlet-triplet window level $1(b)\,^3\Pi_0(v_b,J) \sim 2(A)\,^1\Sigma^+(v_A,J)$. A Coherent model 899-29 single-mode cw titanium sapphire laser (the probe laser) is used to further excite the NaK molecules from the $1(b)\,^3\Pi_0(v_b,J) \sim 2(A)\,^1\Sigma^+(v_A,J)$ window level to various $3\,^3\Pi_0(v_\Pi,J_\Pi)$ levels with $J_\Pi = J\pm1$. The Ti:sapphire laser produces $100-800$ mW of power with a tuning range of $730-920$ nm using the short-wavelength and mid-wavelength optics. The pump and probe lasers counterpropagate through the heat-pipe oven and are focused using 1.0 and 2.0 meter focal length lenses, respectively, such that they spatially overlap at the center of the oven.

Fluorescence from the intermediate $1(b)\,^3\Pi_0(v_b,J) \sim 2(A)\,^1\Sigma^+(v_A,J)$ window level and from the $3\,^3\Pi_0(v_\Pi,J_\Pi)$ upper level is detected at right angles to the laser propagation direction using three detectors. A free standing Hamamatsu R406 photomultiplier tube (PMT), equipped with a $700-1000$ nm bandpass filter, monitors total $2(A)\,^1\Sigma^+(v_A,J) \rightarrow 1(X)\,^1\Sigma^+$ fluorescence and allows the desired $1(b)\,^3\Pi_0(v_b,J) \sim 2(A)\,^1\Sigma^+(v_A,J) \leftarrow 1(X)\,^1\Sigma^+(v_X,J\pm1)$ transition to be located. Once the pump laser frequency is fixed to excite the desired window level, the probe laser frequency is scanned to find $3\,^3\Pi_0(v_\Pi,J_\Pi) \leftarrow 1(b)\,^3\Pi_0(v_b,J) \sim 2(A)\,^1\Sigma^+(v_A,J)$ transitions, which are identified by detecting green $3\,^3\Pi_0 \rightarrow 1(a)\,^3\Sigma^+$ fluorescence using a second free standing PMT (Hamamatsu R928) equipped with appropriate filters. Transitions to rovibrational levels of the $3\,^3\Pi_0$ state can easily be identified because the excitation spectra are inherently Doppler-free, and each $3\,^3\Pi_0(v_\Pi,J_\Pi)$ level displays a characteristic four-peak signature pattern. The pump laser is chopped, and lock-in detection is employed. Removal of an indexer-mounted mirror from the red fluorescence path allows us to record resolved fluorescence using a monochromator/PMT system. In this case, the frequencies of both lasers are fixed to a specific $3\,^3\Pi_0(v_\Pi,J_\Pi) \leftarrow 1(b)\,^3\Pi_0(v_b,J) \sim 2(A)\,^1\Sigma^+(v_A,J) \leftarrow 1(X)\,^1\Sigma^+(v_X,J\pm1)$ double-resonance transition, one of the lasers is chopped, and resolved bound-free $3\,^3\Pi_0 \rightarrow 1(a)\,^3\Sigma^+$ fluorescence is recorded as the monochromator grating is scanned.

The pump laser wavemeter is calibrated using an iodine reference cell and comparing I_2 laser-induced fluorescence lines to those in the reference atlas.[45] The calibration of the probe laser is done using optogalvanic signals from neon transitions in a hollow cathode lamp. Absolute energies of the $3\,^3\Pi_0(v_\Pi,J_\Pi)$ levels obtained in this manner are considered accurate to ~ 0.02 cm^{-1}. However, hyperfine splittings can be determined with much higher precision, typically 0.001 cm^{-1} (30 MHz).

III. ROTATIONAL LEVEL STRUCTURE AND VIBRATIONAL NUMBERING

Transitions to the NaK $3\,^3\Pi$ state are distinguished from those to the nearby $1\,^3\Delta$ and $4\,^3\Sigma^+$ states because they are characterized by a distinctly different rotational line signature pattern, which is shown in Fig. 1 (compare Fig. 4 of Ref. 26 and Fig. 2 of Ref. 27). The angular momentum coupling scheme for the NaK $3\,^3\Pi$ state is intermediate between Hund's case (a) and case (b), but much closer to case (a). Line strengths calculated using the formulas in Table 3.8 of

Ref. 46 indicate that the only $3\,^3\Pi_\Omega(v_\Pi, J_\Pi) \leftarrow 1(b)\,^3\Pi_0(v_b, J_b)$ transitions with significant amplitude are P_{11} and R_{11} with the possible exceptions of P_{21} and R_{21}. However, even these latter transitions should be much weaker than P_{11} and R_{11}, and thus we concentrated on finding the two strong transitions from each of the 16 sets of intermediate state window levels[26,43,47,48] to each 3 $^3\Pi$ vibrational level. The window levels used in this work are listed in Table I of the accompanying Electronic Physics Auxiliary Publication Service (EPAPS) deposit.[49]

For the principal isotopomer ^{23}Na^{39}K, we measured the energies of 290 $3\,^3\Pi_{\Omega=0}$ rotational levels (listed in EPAPS Table II),[49] which span a range of vibrational states initially labeled v_o to v_o+47 (where v_o is the vibrational quantum number of the lowest observed state). The energies of the various rotational levels of each vibrational state were fit to the function $E(v,J)=T_v+B_vJ(J+1)-D_v[J(J+1)]^2$. Values of T_v, B_v, and D_v are listed in EPAPS Table III.[49] [Note that for a few vibrational states, energies of only two rotational levels were recorded, and for those cases no values of D_v are reported. In addition, for mixed levels in the barrier region and cases where the fitted D_v value was unphysical, a linear fit was used.]

Absolute vibrational numbering was established using isotope shifts. We were able to locate one window level $[1(b)\,^3\Pi_0(v=18, J=47) \sim 2(A)\,^1\Sigma^+(v=20, J=47)]$ of the minor isotopomer ^{23}Na^{41}K which is also listed in Table I of the EPAPS file (natural ^{39}K and ^{41}K abundances are 93.26% and 6.73%, respectively).[50] We then carried out a series of standard Dunham expansion fits to the 86 measured energies of ^{23}Na^{39}K $3\,^3\Pi_0$ levels that appeared to be located exclusively in the outer well ($v=v_o$ to v_o+7) using different possible assignments of the lowest observed vibrational level v_o. In these fits, three vibrational and three rotational constants were determined, while the value of Y_{02} was fixed to $-\bar{D}_v$, the weighted average of the individual centrifugal distortion constants determined previously for this set of vibrational states. Energies of ^{23}Na^{41}K $3\,^3\Pi_0$ rovibrational levels were then calculated using the same Dunham coefficients in the formula[51]

$$\mathrm{E}(v,J) = \sum_{i,k} \rho^{i+2k} Y_{i,k} \left(v + \frac{1}{2}\right)^i [J(J+1) - \Omega^2]^k, \tag{1}$$

where

$$\rho = \left[\frac{\mu(^{23}\mathrm{Na}^{39}\mathrm{K})}{\mu(^{23}\mathrm{Na}^{41}\mathrm{K})}\right]^{1/2} \tag{2}$$

and μ is the nuclear reduced mass. Comparison to the measured ^{23}Na^{41}K $3\,^3\Pi_0(v=v_o+6, v_o+7; J=46, 48)$ rovibrational level energies reported in EPAPS Table II (Ref. 49) enabled us to determine conclusively that $v_o=6$ is the correct assignment. Comparison of experimental and simulated $3\,^3\Pi_0(v_\Pi, J_\Pi) \rightarrow 1(a)\,^3\Sigma^+$ bound-free fluorescence and comparison of measured $3\,^3\Pi_0(v_\Pi, J\pm1) \leftarrow 1(b)\,^3\Pi_0(v_b, J)$ excitation line strengths with calculated Franck–Condon factors are also consistent with the assignment $v_o=6$. According to this numbering scheme, the lowest observed rovibrational levels showing any inner well character correspond to $v=14$, consistent with the *ab initio* potential curve of Refs. 52 and 53. The outer well Dunham coefficients, corresponding to the assignment $v_o=6$, are listed in EPAPS Table IV.[49]

IV. IPA POTENTIAL

The standard Rydberg–Klein–Rees (RKR) method cannot be used to map double minimum potentials, such as the NaK 3 $^3\Pi$ state. However, the inverted perturbation approximation (IPA) method[44] can be used to construct a potential curve from the observed level energies. IPA is an iterative approach that aims to find a potential $V(R)$ such that the calculated rovibrational energy levels $E_{\mathrm{calc}}(v,J)$, agree with the experimentally measured energies in the least squares sense. The procedure begins with a "reference potential" $V_0(R)$ whose energies agree roughly with the experimentally determined values. Then, a correction $\delta V(R)$ is determined such that when the Schrödinger equation is solved by applying first-order perturbation theory to the new potential $V(R)=V_0(R)+\delta V(R)$, the calculated eigenvalues match the measured values in the least squares sense. $V(R)$ then becomes the new reference potential, and the procedure is repeated. At each iteration, the values for $\delta V(R)$ are varied at a set of P equidistant points $R_1, R_2, \ldots, R_P$, and intermediate values are determined by cubic spline.

The calculations reported here use a slightly modified version of the publicly available IPA code.[44] We simplified the input files and incorporated subroutines from the program LEVEL (Ref. 54) to calculate the rovibrational energy levels of the reference potential.

The convergence of the IPA method is greatly improved if the initial reference potential $V_0(R)$ is reasonably close to the actual potential. We used a modified form of the theoretical NaK $3\,^3\Pi$ potential of Magnier *et al.*,[53] $V_0(R) = A[U(R)-U(\infty)]+E[\mathrm{Na}(3S)+K(3D)]+D_e(X\,^1\Sigma^+)$, where $U(R)$ and $U(\infty)$ are the theoretical potential of Ref. 53 at R and at the asymptotic limit, respectively, $E[\mathrm{Na}(3S)+\mathrm{K}(3D)]=21\,535.35\ \mathrm{cm}^{-1}$ is the known atomic energy[55] at the dissociation limit (relative to $E[\mathrm{Na}(3S)+\mathrm{K}(4S)]$), $D_e(X\,^1\Sigma^+)=5173.78\ \mathrm{cm}^{-1}$ is the ground state dissociation energy from Ref. 56, and $A=1.0318$ is a constant chosen such that the minimum of the outer well agreed with the $T_e=Y_{00}$ value obtained in the previously described Dunham fit (corresponding to a downward shift of the outer well minimum by $\sim 66.4\ \mathrm{cm}^{-1}$). Using this $V_0(R)$, the standard deviation of the differences between the measured and calculated rovibrational energies is $\sim 3.95\ \mathrm{cm}^{-1}$.

After each iteration, level energies were calculated from the new potential curve $V(R)$ and compared with the experimental energies. In addition, we plotted each iteration of the IPA potential to ensure that no unphysical "wiggles" had been introduced. Since IPA adjusts the potential at a set of grid points, such oscillations or wiggles become more likely as the density of grid points is increased. In the present case, we started with a relatively coarse grid ($P=9$) and slowly increased the number in subsequent iterations, eventually reaching $P=28$.

The IPA method has a tendency to introduce unphysical wiggles, especially in the first few iterations. Since the low-

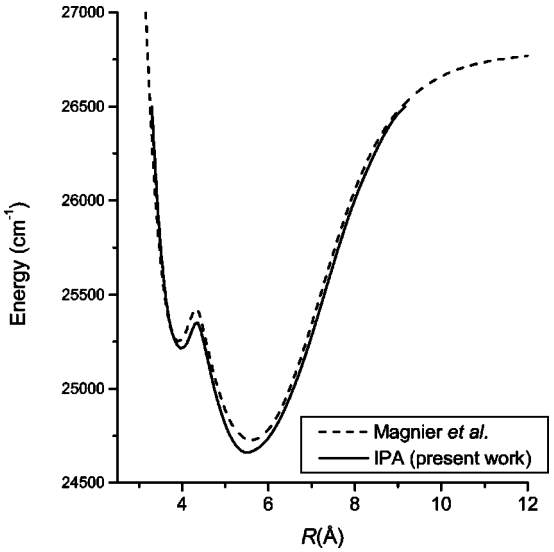

FIG. 2. Comparison of the experimental NaK 3 $^3\Pi_0$ potential energy curve determined in this work (solid line) with the theoretical potential of Magnier *et al.* (Refs. 52 and 53) (dashed line).

est experimental energies correspond to $v_o=6$, there is insufficient information to map the region of the potential near the bottom of the outer well. Thus, the program could introduce wiggles into the lower portion of the outer well, while still reproducing the experimental energies with good accuracy. To eliminate this problem and prevent such unphysical results, we used the outer well Dunham coefficients fitted to the experimental $v=6-13$ data points to extrapolate the $E(v,J)$ values for $v=0-5$, and these extrapolated energies were added to the database and used in the IPA iterations.

The publicly available IPA code[44] also allows the user to freeze the potential at some of the grid points while varying it at others. In the early stages of the iteration process, we allowed all points to vary. However, in later iterations, we often fixed either the lower part of the outer well or the long-range outer wall of the potential in order to improve the agreement between the experimental and calculated energies. In the end, 549 experimentally measured 3 $^3\Pi_0(v,J)$ $\leftarrow 1(b)$ $^3\Pi_0 \sim 2(A)$ $^1\Sigma^+$ transition energies, representing 264 3 $^3\Pi_0$ rovibrational levels with v ranging from 6 to 53, were used in the fit. Seventy of the original 619 transition energies [representing 26 of the 3 $^3\Pi_0(v,J)$ rovibrational levels all with $v \geqslant 32$] were omitted from the analysis because they appeared to be strongly perturbed by nearby levels of the 4 $^3\Pi$ state. A total of 25 iterations was carried out to produce the final IPA potential, which is given in Table V of the EPAPS file.[49] We believe this IPA potential energy curve represents the best compromise between accurately reproducing the measured level energies and maintaining a reasonably smooth curve. The standard deviation of the energies calculated using the final IPA potential and the experimental energies is 0.24 cm^{-1}. Figure 2 shows a comparison of the IPA potential obtained in this work and the theoretical potential of Magnier *et al.*[53] The R values of the experimental IPA potential inner and outer well minima and barrier maximum agree with those of the theoretical potential to within $\sim$0.10 Å, and the corresponding energies of these extrema are between 35 and 75 cm^{-1} lower for the IPA curve than for the theoretical potential. This excellent agreement provides further evidence of the high quality of these theoretical potentials.

It should be noted that levels of the 3 $^3\Pi$ state are affected by nonadiabatic coupling with the 4 $^3\Pi$ state. However, 3 $^3\Pi$ rovibrational levels lying below the minimum of the 4 $^3\Pi$ state and higher energy rovibrational levels that are more than 10 or 20 cm^{-1} from the nearest 4 $^3\Pi$ level with the same J are not strongly affected and are typically shifted down by $\sim$1 cm^{-1} or less.[57] The IPA method accommodates these small shifts by slight adjustment of the potential, such that the present IPA potential, without nonadiabatic corrections, reproduces these energies to the stated 0.24 cm^{-1} accuracy. However, 3 $^3\Pi$ levels lying near 4 $^3\Pi$ levels of the same J [those marked with an asterisk in EPAPS Table II (Ref. 49)] are more strongly affected by nonadiabatic coupling and these levels were excluded from the IPA fit. A complete analysis of the 4 $^3\Pi$ and 3 $^3\Pi$ states, including nonadiabatic coupling effects, is in progress and will be presented in a future publication.[57]

V. INNER AND OUTER WELL LEVELS

The major characteristic of the 3 $^3\Pi$ state potential curve is its double minimum structure, which results from an avoided curve crossing with the nearby 4 $^3\Pi$ state. *Ab initio* calculations[57] show that the adiabatic 3 $^3\Pi$ double minimum state results primarily from the interaction of three diabatic states, of which two are approximately parallel to the NaK^+ ground state, while the third is nearly parallel to the first excited state of NaK^+. The inner well of the adiabatic potential is dominated by one diabatic state dissociating to the $Na(3S)+K(5P)$ atomic limit, which has the character of an ion-core ground state. The electronic wave function associated with the outer well has contributions from two diabatic states, one with the character of an ion-core ground state dissociating to the $Na(3S)+K(3D)$ limit and one with the character of an ion-core excited state dissociating to the $Na(3P)+K(4S)$ atomic limit. Hence we expect the vibrational, rotational, fine, and hyperfine splittings to differ in different regions of the double minimum potential.

Figure 3 shows a plot of the rotational constant B_v versus v, demonstrating that the 3 $^3\Pi$ state can be divided into three distinct regions: those vibrational levels located exclusively in the outer well ($0 \leqslant v \leqslant 13$), those in the barrier region where the wave function has some amplitude in both the inner and the outer wells ($14 \leqslant v \leqslant 21$), and those above the barrier ($v \geqslant 22$). Since the rotational constant B_v is proportional to the average of R^{-2} for a given vibrational level, significantly different values of B_v are expected for rovibrational levels located in the inner well compared to those located in the outer well, and this is reflected in the bifurcation of the B_v versus v plot in the region $14 \leqslant v \leqslant 21$.

Figure 4 shows measured rovibrational energies $E(v,J)$ in the barrier region plotted versus $J(J+1)$. The vibrational quantum number is associated with the number of nodes in the radial wave function. As a result, the level $v=14$ has inner well character at low $J(\leqslant 27)$ and outer well character

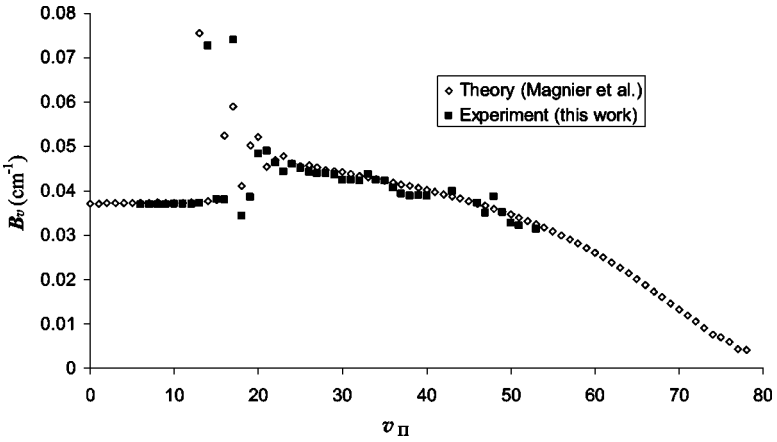

FIG. 3. Experimental NaK 3 $^3\Pi_0$ state rotational constants B_v obtained in this work (squares) compared to those calculated from the theoretical potential of Magnier *et al.* (Refs. 52 and 53) (diamonds).

at high J. Similarly, $v=15$ has outer well character for $J \leqslant 27$, inner well character for $27<J<43$, and outer well character for $J \geqslant 43$. Figure 5 shows radial wave functions, calculated using the program LEVEL,[54] for some rovibrational levels superimposed on plots of the 3 $^3\Pi_0$ IPA electronic potential for the appropriate J [i.e., $V(J)=V(J=0)+\hbar^2 J(J+1)/2\mu R^2$]. It can be seen that for the nearly degenerate $v=14$ and 15, $J=27$ levels (see Fig. 4), the radial wave functions have large amplitudes in both inner and outer well regions. However, for levels more removed from the crossing in Fig. 4 (i.e., $J=16$ and $J=39$), the wave functions are much more localized in either the inner or the outer well region.

Inner and outer well rovibrational levels are readily identified by their hyperfine structure, because inner well rovibrational levels display larger hyperfine splittings than outer well levels (see Fig. 6). Since the Fermi contact interaction $b_F \mathbf{I}\cdot\mathbf{S}$ is the dominant contribution to the hyperfine structure of all electronic states of the alkali diatomic molecules,[42,58–60] we expect the coupling constant b_F to be larger for inner well than for outer well rovibrational levels. A complete theoretical model explaining these results in terms of diabatic potentials is underway and will be presented in Ref. 57. In cases where levels with the same J are nearly degenerate (i.e., $v=14$ and 15, $J=27$—see Fig. 4), the radial wave functions have large amplitudes in both inner and outer well regions, and the observed hyperfine splittings are intermediate between those of the pure inner and pure outer well levels. The changes of the splittings near the crossings shown in Fig. 4 are related to the coupling of inner and outer well levels, which in turn is related to the barrier tunneling probability. We believe that the dependence of these hyperfine splittings on J is a sensitive indicator of the 3 $^3\Pi_0$ barrier height, and our analysis of this effect will be presented in a later publication.

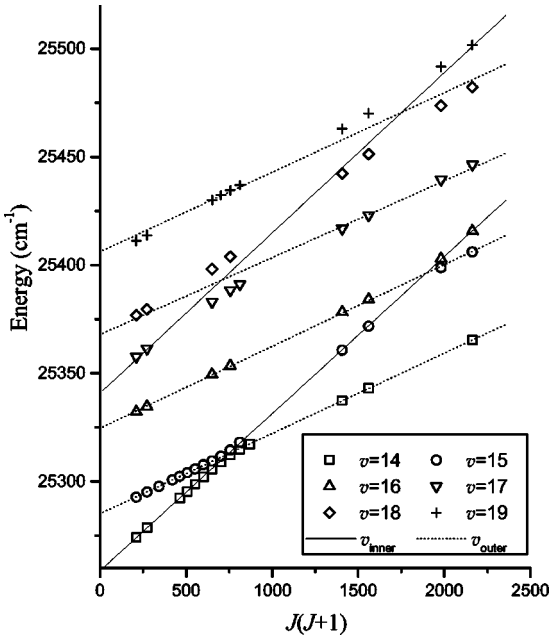

FIG. 4. $E(v,J)$ vs $J(J+1)$ for NaK 3 $^3\Pi_0$ rovibrational levels in the range $14 \leqslant v \leqslant 19$. Each symbol denotes those rovibrational levels with a specific number of nodes (14–19) in the radial wave function. The solid lines represent series of levels where the amplitude of the vibrational wave function is located mostly in the inner well. Similarly, the dotted lines denote those rovibrational levels for which the wave function amplitude is located mostly in the outer well.

VI. BOUND-FREE SPECTRA

Resolved bound-free 3 $^3\Pi_0(v,J) \rightarrow 1(a)$ $^3\Sigma^+$ fluorescence spectra were recorded for various rovibrational levels in the outer well and above the barrier (see Fig. 7). To obtain these spectra, both the pump and probe laser frequencies were fixed to populate a particular upper state level 3 $^3\Pi_0(v,J)$ and the monochromator was scanned in frequency. The 3 $^3\Pi_0 - 1(a)$ $^3\Sigma^+$ difference potential is not a monotonic function of R, so an observed bound-free spectrum does not reflect the number of nodes in the bound state radial wave function (cf. Fig. 4 of Ref. 27). Instead, the 3 $^3\Pi_0(v,J) \rightarrow 1(a)$ $^3\Sigma^+$ bound-free spectra display interference structure.[61] Nevertheless, quantum mechanical simulations of these spectra calculated using the program BCONT (Ref. 62) with the 3 $^3\Pi_0$ IPA potential determined in this work, the composite experimental $1(a)$ $^3\Sigma^+$ potential of Refs. 63 and 64, and the theoretical 3 $^3\Pi_0 \rightarrow 1(a)$ $^3\Sigma^+$ transition dipole moment of Ref. 53 [see Figs. 7(b) and 7(d)] reproduce the bound-free parts of the spectra reasonably well. (Note that the short wavelength end of the 3 $^3\Pi_0 \rightarrow 1(a)$ $^3\Sigma^+$ fluorescence band consists of transitions into bound levels of the lower state that are not simulated by the BCONT program.) Unfortunately, weak Franck–Condon factors for pumping to 3 $^3\Pi_0$ inner well levels from the $1(b)$ $^3\Pi_0$ state, coupled with

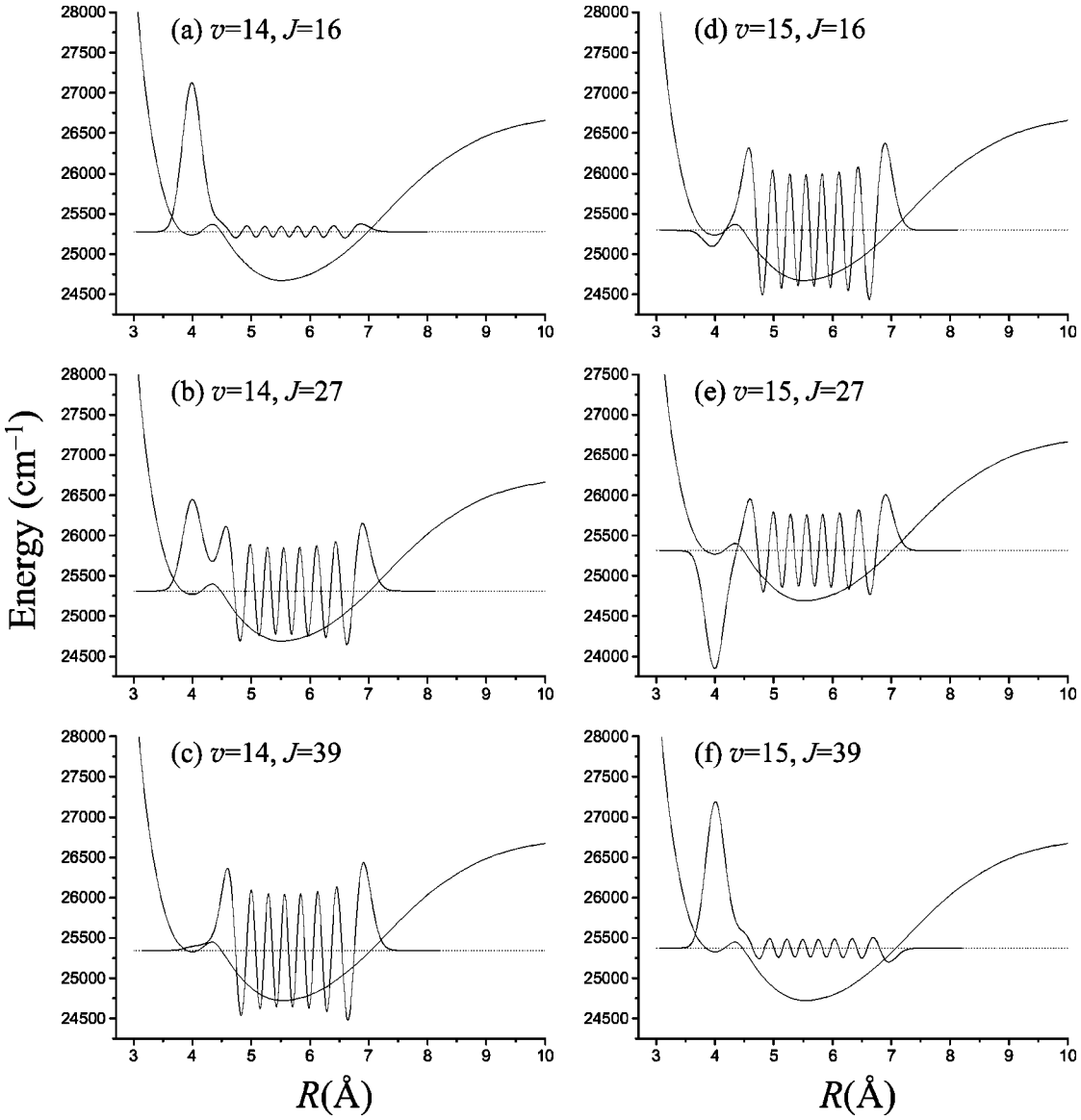

FIG. 5. Vibrational (radial) wave functions for some rovibrational levels depicted in Fig. 4. Each wave function is superimposed on the corresponding plot of the $3\,^3\Pi_0$ electronic potential curve. (a) $v=14$, $J=16$, (b) $v=14$, $J=27$, (c) $v=14$, $J=39$, (d) $v=15$, $J=16$, (e) $v=15$, $J=27$, (f) $v=15$, $J=39$.

the small $3\,^3\Pi_0 \rightarrow 1(a)\,^3\Sigma^+$ transition dipole moment at small R, reduce the bound-free fluorescence intensity from inner well levels to less than our detection threshold. Mixed inner/outer well levels, such as $v=14$, 15, $J=27$, exhibit bound-free spectra consistent with their outer well amplitude.

VII. HYPERFINE STRUCTURE AND SPIN–ORBIT INTERACTION

The Fermi contact interaction has been found to dominate the hyperfine structure of all alkali molecules.[42,58–60] For NaK, it has also been found that the contribution from the sodium nucleus ($I=3/2$) is much more important than that from the potassium nucleus because the magnetic moment of the sodium nucleus is significantly larger than that of potassium and because the electron spin density at the sodium nucleus is also larger.[26,27,43] Under these conditions, Burns *et al.*[43] demonstrated that rovibrational levels of a $^3\Pi_{\Omega=0}$ state split into four hyperfine levels ($F=J-\frac{3}{2}$, $J-\frac{1}{2}$, $J+\frac{1}{2}$, and $J+\frac{3}{2}$), and if the $^3\Pi$ state follows a coupling scheme intermediate between Hund's case (a) and Hund's case (b), then the average hyperfine splitting of adjacent F levels of the $\Omega=0$ component $\Delta E^0_{\mathrm{hfs}}$ is well represented by

$$\Delta E^0_{\mathrm{hfs}} = b_{\mathrm{F}} \frac{\chi}{\sqrt{1+\chi^2}}, \tag{3}$$

where χ is a dimensionless parameter that determines where the coupling scheme lies on the continuum between Hund's case (a) and Hund's case (b):

$$\chi = \frac{2B_v\left(J+\frac{1}{2}\right)}{\Lambda A_v}. \tag{4}$$

Here B_v and A_v are the rotational constant and spin–orbit constant, respectively, and $\Lambda=1$ for a Π state. Equation (3) is an approximation to the results of the more accurate full matrix diagonalization method outlined in Ref. 27. The va-

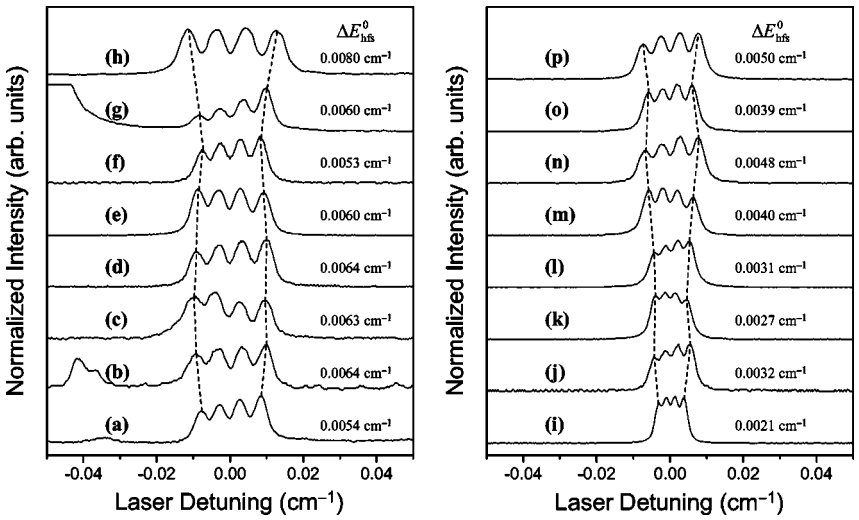

FIG. 6. 3 $^3\Pi_0$ hyperfine splittings for rovibrational levels near the crossing of the lowest dotted and solid lines in Fig. 4. Traces (a)–(h) show hyperfine splittings for nominally "inner well" rovibrational levels [(a) $v=14$, $J=16$, (b) $v=14$, $J=23$, (c) $v=14$, $J=24$, (d) $v=14$, $J=25$, (e) $v=14$, $J=26$, (f) $v=14$, $J=27$, (g) $v=15$, $J=28$, and (h) $v=15$, $J=39$]. Traces (i)–(p) show the hyperfine splittings for nominally outer well rovibrational levels [(i) $v=15$, $J=16$, (j) $v=15$, $J=23$, (k) $v=15$, $J=24$, (l) $v=15$, $J=25$, (m) $v=15$, $J=26$, (n) $v=15$, $J=27$, (o) $v=14$, $J=28$, and (p) $v=14$, $J=39$].

lidity of the approximation requires that the hyperfine splitting be small compared to the fine structure and rotational splittings.

Equation (3) can be put into the convenient form

$$\frac{1}{(\Delta E^0_{\rm hfs})^2}=\frac{1}{(b_{\rm F})^2}\left(1+\frac{1}{\chi^2}\right)=\frac{1}{(b_{\rm F})^2}+\left(\frac{\Lambda A_v}{2B_v b_{\rm F}\left(J+\frac{1}{2}\right)}\right)^2, \tag{5}$$

which shows that a plot of $(\Delta E^0_{\rm hfs})^{-2}$ versus $\left(J+\frac{1}{2}\right)^{-2}$ for the measured rotational levels of a given vibrational state should, under appropriate conditions, yield a straight line whose intercept is $(b_{\rm F})^{-2}$ and whose slope to intercept ratio is $(\Lambda A_v/2B_v)^2$. If the rotational constant B_v is known, the spin–orbit interaction constant A_v can be determined, even if data from only one fine structure component ($\Omega=0$) are available. We carried out an analysis of this type using our NaK 3 $^3\Pi_0$ data. Unfortunately, small uncertainties in the measured hyperfine splittings (due to small perturbations as well as limited experimental resolution) result in relatively large uncertainties in the fitted values of $b_{\rm F}$ and A_v.

Conversely, if the values of both B_v and A_v are known, the Fermi contact constant can be determined directly from the measured hyperfine splittings of a single rovibrational level using Eq. (3) or the full matrix diagonalization method. For a $^3\Pi$ state intermediate between Hund's case (a) and case (b), Kovács[46] has shown that the splitting ΔE between the $\Omega=2$ and $\Omega=0$ fine structure components of a particular rovibrational level (v,J) is given approximately by the expression

$$\begin{aligned}\Delta E &\equiv E(v,J,\Omega=2)-E(v,J,\Omega=0)\\ &\approx 2B_v[y_1+4J(J+1)]^{1/2}\end{aligned} \tag{6}$$

with

$$y_1=\Lambda^2\frac{A_v}{B_v}\left(\frac{A_v}{B_v}-4\right)+\frac{4}{3}. \tag{7}$$

Thus A_v can be obtained directly from this splitting:

$$A_v=\frac{\Delta E}{2\Lambda}\left\{1-\frac{16B_v^2}{\Delta E^2}\left[J(J+1)+\frac{1}{3}-\Lambda^2\right]\right\}^{1/2}+2B_v. \tag{8}$$

We note that in the near case (a) limit ($A_v \gg B_v J$) Eq. (6) yields $\Delta E \approx 2\Lambda A_v$ with a correction term that grows with $J(J+1)$. Therefore a value for A_v can be obtained by extrapolating a plot of ΔE versus $J(J+1)$ to $J=0$. Ross *et al.*[65] used an analysis of this type to determine the spin–orbit interaction constants of the NaK $1(b)$ $^3\Pi$ state from the $\Omega=2$ and $\Omega=1$ level splittings. We have checked that the approximate formula Eq. (6) agrees with full matrix diagonalization results to better than 0.1% for values of A_v, B_v, and J relevant to the present study of the NaK 3 $^3\Pi$ state.

In the present work, we have been able to identify two $\Omega=2$ window levels: $1(b)$ $^3\Pi_2(v_b=20,J=32)\sim 2(A)$ $^1\Sigma^+(v_A=23,J=32)$ and $1(b)$ $^3\Pi_2(v_b=17,J=45)\sim 2(A)$ $^1\Sigma^+(v_A=19,J=45)$—see EPAPS Table I.[49] Using these, we have observed 3 $^3\Pi_2(v,J=31,33,44,46)$ levels for a number of different v's. The 3 $^3\Pi_0(v,J=44,46)$ levels were also observed, thus allowing direct determination of ΔE for those J values, and hence of A_v using Eq. (8). The 3 $^3\Pi_0(v,J=31,33)$ level energies were not experimentally accessible to us with our current set of $1(b)$ $^3\Pi_0(v_b,J)\sim 2(A)$ $^1\Sigma^+(v_A,J)$ window levels, and so we determined these energies (with somewhat less accuracy) from the fitted T_v, B_v, and whenever possible D_v constants. For a given v, the best value for A_v was determined from the weighted mean of the individual values obtained from the 3 $^3\Pi_2$ lines.[66] The uncertainties in the individual A_v values are dominated by the uncertainty in ΔE, which is 0.02 cm^{-1} for the $J=44$ and 46 data and slightly more for the $J=31$ and 33 data.

The weighted mean A_v values were then used, together with the B_v values from EPAPS Table III, to determine $b_{\rm F}$ values for all 3 $^3\Pi_{\Omega=0}$ rotational levels of a given v, using either Eq. (3) or the more accurate matrix diagonalization method. Values from Eq. (3) were found to be systematically too high by typically a few percent, and so we report weighted mean $b_{\rm F}$ values obtained from matrix diagonalization. The statistical uncertainty in individual $b_{\rm F}$ values is dominated by the 0.0003 cm^{-1} uncertainty in the average

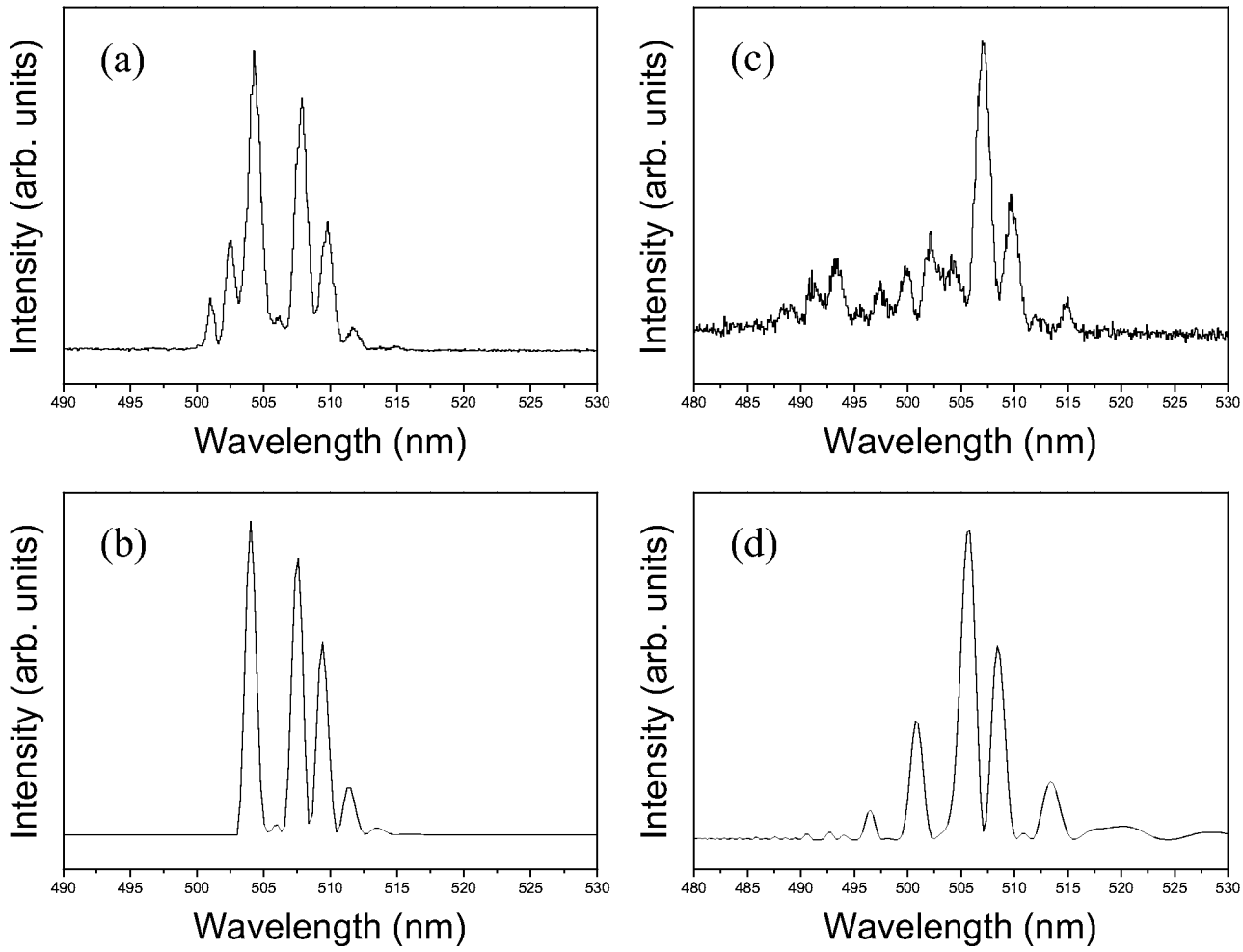

FIG. 7. (a) 3 $^3\Pi_0 \rightarrow 1(a)$ $^3\Sigma^+$ bound-free spectrum associated with a 3 $^3\Pi_0$ pure outer well rovibrational level ($v=10$, $J=27$). (b) Simulated 3 $^3\Pi_0(v=10, J=27) \rightarrow 1(a)$ $^3\Sigma^+$ spectrum calculated using the program BCONT (Ref. 62) with the NaK 3 $^3\Pi_0$ IPA potential curve determined in this work, the $1(a)$ $^3\Sigma^+$ potential from Refs. 63 and 64, and the theoretical 3 $^3\Pi_0 \rightarrow 1(a)$ $^3\Sigma^+$ transition dipole moment of Ref. 53. Note: The first two peaks in the experimental bound-free spectrum located at 501.0 and 502.5 nm correspond to 3 $^3\Pi_0(v=10, J=27) \rightarrow 1(a)$ $^3\Sigma^+$ bound-bound transitions that are not evaluated in the simulated spectrum. (c) 3 $^3\Pi_0 \rightarrow 1(a)$ $^3\Sigma^+$ spectrum associated with a 3 $^3\Pi_0$ level located above the barrier ($v=40, J=44$). (d) Simulated 3 $^3\Pi_0(v=40, J=44) \rightarrow 1(a)$ $^3\Sigma^+$ bound-free spectrum.

hyperfine splittings, but also depends to a lesser extent on the uncertainties in A_v and B_v. The A_v and b_F values obtained in this manner are plotted in Fig. 8 as a function of v along with their respective uncertainties, and they are listed in EPAPS Table III.[49] In cases where $\Omega=2$ data were not available, fits of the $\Omega=0$ data were carried out using Eq. (5) or the matrix equivalent. However the uncertainties are sufficiently large that these results are not given here but will be reported at a later date in Ref. 67.

The most interesting result is that b_F and A_v values are different for different regions of the 3 $^3\Pi$ double minimum potential. Predominantly inner well levels have larger b_F values and smaller A_v values than predominantly outer well levels. For levels located above the barrier, b_F gradually increases and A_v decreases as a function of v. For v in the range 35–51, b_F is close to the value 0.01 cm^{-1}, which is similar to that found for other electronic states of NaK with ground state ion-core character.[26,27,39–43] Asymptotically, we expect b_F to approach 443 MHz=0.0148 cm^{-1}, which is half the value for atomic sodium in the ground state. A discussion of the variation of b_F with v in terms of diabatic states will be presented in Ref. 57.

Our expectation is that, for large v, A_v should asymptotically approach the value associated with the fine structure splitting of the potassium atom in the atomic dissociation limit K($3D$)+Na($3S$). Using standard formulas to evaluate $A\,\mathbf{L}\cdot\mathbf{S}$ for the levels with $\mathbf{J}=\mathbf{L}+\mathbf{S}$, it is easily shown that

$$\Delta E = E_{5/2} - E_{3/2} = \tfrac{5}{2}A. \tag{9}$$

Since the experimental value of ΔE is -2.33 cm^{-1} (the levels are inverted),[55] we expect the limiting value of A_v to be about -1 cm^{-1}. Figure 8 shows that A_v is decreasing as v increases, so it is plausible that A_v could pass through zero and approach -1 cm^{-1}.

VIII. CONCLUSIONS

Using the perturbation-facilitated optical-optical double-resonance method, we have measured the energies of 290 rovibrational levels spanning 85% of the well depth of the NaK 3 $^3\Pi_0$ electronic potential. We identified one window level of the minor isotopomer $^{23}Na^{41}K$, which allowed us to calculate isotope shifts of the 3 $^3\Pi_0$ level energies and thereby establish the absolute vibrational numbering for this

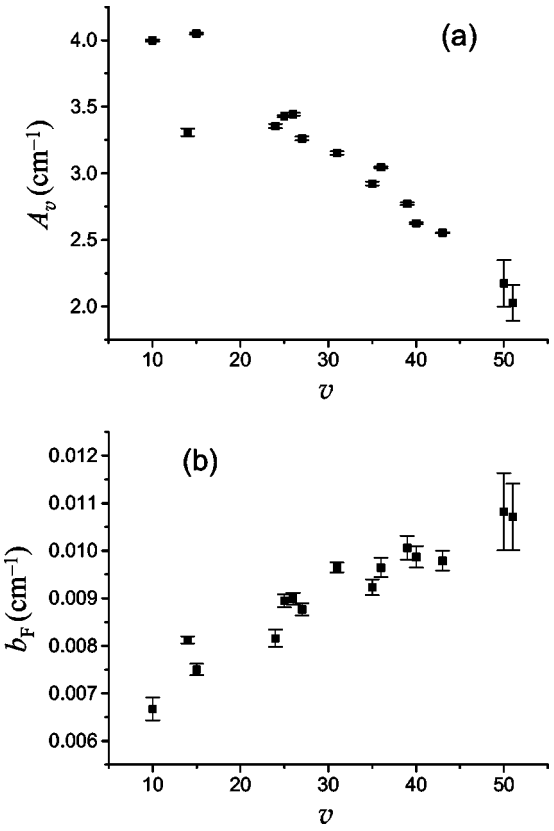

FIG. 8. (a) NaK 3 $^3\Pi$ spin–orbit interaction constant A_v as a function of vibrational quantum number v. The values were determined from the splittings between the $\Omega=0$ and $\Omega=2$ fine structure components of a given 3 $^3\Pi$ rovibrational level [Eq. (8)]. Note that inner and outer well vibrational assignments were chosen to correspond to that at low J [i.e., the A_v value plotted for $v=14$ corresponds to an average over the lowest inner well state (actually comprising levels belonging to $v=14$, 15, and 16 in the global numbering scheme) while the value plotted at $v=15$ corresponds to an average over the lowest outer well state in this overlap region—see Fig. 4]. (b) Fermi contact constant b_F for the NaK 3 $^3\Pi_0$ state as a function of vibrational quantum number.

state. The inverted perturbation approximation (IPA) method was used to construct a potential curve from the experimental data, which reproduces the experimental energies used in the fit with a rms deviation of ~ 0.24 cm^{-1}. Our results are in good agreement with the theoretical potential of Magnier *et al.*[52,53]

The double minimum nature of the 3 $^3\Pi$ electronic state, which is caused by an avoided curve crossing between the 3 $^3\Pi$ and nearby 4 $^3\Pi$ electronic states, leads to many interesting physical phenomena. The vibrational spacing ΔG_v, rotational constant B_v, hyperfine splittings $\Delta E^0_{\mathrm{hfs}}$, spin–orbit constant A_v, and Fermi contact constant b_F all vary as a function of vibrational quantum number and all exhibit different values and dependencies in different regions of the potential. Due to avoided curve crossings, the 3 $^3\Pi$ state has significant contributions from three different diabatic states, which are responsible for the variations in the above-mentioned quantities. Two of these three diabatic states also contribute to the 4 $^3\Pi$ electronic state, which is a *V*-shaped potential. Experimental and theoretical work on this latter state is underway and demonstrates that low-lying levels of the 4 $^3\Pi$ state are strongly perturbed by nonadiabatic coupling with nearby levels of the 3 $^3\Pi$ state.[57]

ACKNOWLEDGMENTS

This work was supported by the National Science Foundation Grant No. PHY-0244767. L.M. is supported by a NSF graduate fellowship. U.O. was supported by the NSF REU site grant in the Department of Physics at Lehigh University and the Lehigh Center for Optical Technologies.

[1] X. Xie and R. W. Field, J. Mol. Spectrosc. **117**, 228 (1986).
[2] Li Li, T. An, T.-J. Whang, A. M. Lyyra, W. C. Stwalley, R. W. Field, and R. A. Bernheim, J. Chem. Phys. **96**, 3342 (1992).
[3] D. S. Chen, L. Li, X. T. Wang, Li Li, Q. Hui, H. Ma, L. Q. Li, X. Y. Xu, and D. Y. Chun, J. Mol. Spectrosc. **161**, 7 (1993).
[4] A. Yiannopoulou, B. Ji, Li Li, M. Li, K. Urbanski, A. M. Lyyra, W. C. Stwalley, and G.–H. Jeung, J. Chem. Phys. **101**, 3581 (1994).
[5] A. Yiannopoulou, K. Urbanski, A. M. Lyyra, Li Li, B. Ji, J. T. Bahns, and W. C. Stwalley, J. Chem. Phys. **102**, 3024 (1995).
[6] Li Li, A. Yiannopoulou, K. Urbanski, A. M. Lyyra, B. Ji, W. C. Stwalley, and T. An, J. Chem. Phys. **105**, 6192 (1996); **106**, 8626(E) (1997).
[7] C. Linton, F. Martin, A. J. Ross, I. Russier, P. Crozet, A. Yiannopoulou, Li Li, and A. M. Lyyra, J. Mol. Spectrosc. **196**, 20 (1999).
[8] Li Li and A. M. Lyyra, Spectrochim. Acta, Part A **55**, 2147 (1999).
[9] X. Dai, J. O. Clevenger, Y. Liu, M. Song, J. Shang, D. Chen, R. W. Field, and Li Li, J. Mol. Spectrosc. **200**, 120 (2000).
[10] G. Lazarov, A. M. Lyyra, and Li Li, J. Mol. Spectrosc. **205**, 73 (2001).
[11] Li Li and R. W. Field, J. Phys. Chem. **87**, 3020 (1983).
[12] Li Li and R. W. Field, J. Mol. Spectrosc. **117**, 245 (1986).
[13] T.-J. Whang, W. C. Stwalley, Li Li, and A. M. Lyyra, J. Mol. Spectrosc. **155**, 184 (1992).
[14] Y. Liu, J. Li, M. Xue, D. Chen, Li Li, and G.-H. Jeung, J. Chem. Phys. **103**, 7213 (1995).
[15] B. Ji, C.-C. Tsai, Li Li, T.-J. Whang, A. M. Lyyra, H. Wang, J. T. Bahns, W. C. Stwalley, and R. J. LeRoy, J. Chem. Phys. **103**, 7240 (1995).
[16] J. Li, Y. Liu, H. Gao, M. Xue, D. Chen, and Li Li, J. Mol. Spectrosc. **175**, 13 (1996).
[17] Y. Liu, J. Li, H. Gao, D. Chen, Li Li, R. W. Field, and A. M. Lyyra, J. Chem. Phys. **108**, 2269 (1998).
[18] G. Lazarov, A. M. Lyyra, Li Li, and J. Huennekens, J. Mol. Spectrosc. **196**, 259 (1999).
[19] Y. Liu, B. Ji, A. S.-C. Cheung, W. C. Stwalley, R. W. Field, A. M. Lyyra, and Li Li, J. Chem. Phys. **115**, 3647 (2001).
[20] P. Yi, X. Dai, J. Li, Y. Liu, Li Li, V. B. Sovkov, and V. S. Ivanov, J. Mol. Spectrosc. **225**, 33 (2004).
[21] Y. Liu, Li Li, G. Lazarov, A. Lazoudis, A. M. Lyyra, and R. W. Field, J. Chem. Phys. **121**, 5821 (2004).
[22] Li Li, A. M. Lyyra, W. T. Luh, and W. C. Stwalley, J. Chem. Phys. **93**, 8452 (1990).
[23] J. T. Kim, H. Wang, C. C. Tsai, J. T. Bahns, W. C. Stwalley, G. Jong, and A. M. Lyyra, J. Chem. Phys. **102**, 6646 (1995); **103**, 9891(E) (1995).
[24] G. Zhao, W. T. Zemke, J. T. Kim, B. Ji, H. Wang, J. T. Bahns, W. C. Stwalley, Li Li, A. M. Lyyra, and C. Amiot, J. Chem. Phys. **105**, 7976 (1996).
[25] J. Magnes, E. Ahmed, C. Goldberg, A. M. Lyyra, S. Magnier, M. Aubert-Frécon, Y. Liu, and Li Li, J. Mol. Spectrosc. **221**, 72 (2003).
[26] J. Huennekens, I. Prodan, A. Marks, L. Sibbach, E. Galle, T. Morgus, and Li Li, J. Chem. Phys. **113**, 7384 (2000).
[27] P. Burns, L. Sibbach-Morgus, A. D. Wilkins, F. Halpern, L. Clarke, R. D. Miles, Li Li, A. P. Hickman, and J. Huennekens, J. Chem. Phys. **119**, 4743 (2003).
[28] P. Yi, M. Song, Y. Liu, A. M. Lyyra, and Li Li, Chem. Phys. Lett. **349**, 426 (2001).
[29] Li Li, A. Lazoudis, P. Yi, Y. Liu, J. Huennekens, R. W. Field, and A. M. Lyyra, J. Chem. Phys. **116**, 10704 (2002).
[30] L.-E. Berg, M. Beutter, and T. Hansson, Chem. Phys. Lett. **253**, 327 (1996).
[31] T. Hansson, J. Phys. B **32**, 1997 (1999).
[32] J. P. Woerdman, Opt. Commun. **26**, 216 (1978).
[33] A. Kopystyńska and P. Kowalczyk, Opt. Commun. **28**, 78 (1979).
[34] G. Pichler, J. T. Bahns, K. M. Sando, W. C. Stwalley, D. D. Konowalow, Li Li, R. W. Field, and W. Müller, Chem. Phys. Lett. **129**, 425 (1986).
[35] S. Milošević and G. Pichler, Z. Phys. D: At., Mol. Clusters **1**, 223 (1986).
[36] W.-T. Luh, J. T. Bahns, A. M. Lyyra, K. M. Sando, P. D. Kleiber, and W. C. Stwalley, J. Chem. Phys. **88**, 2235 (1988).

[37]P. Kowalczyk, S. Milošević, and G. Pichler, Z. Phys. D: At., Mol. Clusters **11**, 213 (1989).
[38]D. Xing, K. Ueda, and H. Takuma, Appl. Phys. Lett. **58**, 1701 (1991).
[39]P. Kowalczyk, B. Krüger, and F. Engelke, Chem. Phys. Lett. **147**, 301 (1988).
[40]P. Kowalczyk, J. Chem. Phys. **91**, 2779 (1989).
[41]M. Baba, K. Nishizawa, N. Yoshie, K. Ishikawa, and H. Katô, J. Chem. Phys. **96**, 955 (1992).
[42]K. Ishikawa, T. Kumauchi, M. Baba, and H. Katô, J. Chem. Phys. **96**, 6423 (1992).
[43]P. Burns, A. D. Wilkins, A. P. Hickman, and J. Huennekens, J. Chem. Phys. **122**, 074306 (2005).
[44]A. Pashov, W. Jastrzębski, and P. Kowalczyk, Comput. Phys. Commun. **128**, 622 (2000).
[45]S. Gerstenkorn and P. Luc, *Atlas du Spectre D'Absorption de la Molécule D'Iode* (Centre National de la Recherche Scientifique, Paris, 1978).
[46]I. Kovács, *Rotational Structure in the Spectra of Diatomic Molecules* (American Elsevier, New York, 1969).
[47]M. Masters, J. Huennekens, W.-T. Luh, Li Li, A. M. Lyyra, K. Sando, V. Zafiropulos, and W. C. Stwalley, J. Chem. Phys. **92**, 5801 (1990).
[48]H. Sun and J. Huennekens, J. Chem. Phys. **97**, 4714 (1992).
[49]See EPAPS Document No. E-JCPSA6-122-023515 for five tables of related information. A direct link to this document may be found in the online article's HTML reference section. The document may also be reached via the EPAPS homepage (http://www.aip.org/pubservs/epaps.html) or from ftp.aip.org in the directory /epaps/. See EPAPS homepage for more information.
[50]National Institute of Standards and Technology (NIST). 11 November 2004, http://physics.nist.gov/PhysRefData/Handbook/Tables/potassiumtable1.htm
[51]R. J. LeRoy, DParFit 3.2: A Computer Program for Fitting Diatomic Molecule Spectral Data to Parameterized Level Energy Expressions, Chemical Physics Research Report No. CP-658R, University of Waterloo, 2004.
[52]S. Magnier and Ph. Millié, Phys. Rev. A **54**, 204 (1996).
[53]S. Magnier, M. Aubert-Frécon, and Ph. Millié, J. Mol. Spectrosc. **200**, 96 (2000).
[54]R. J. LeRoy, LEVEL 7.5: A Computer Program for Solving the Radial Schrödinger Equation for Bound and Quasibound Levels, Chemical Physics Research Report No. CP-655, University of Waterloo, 2002.
[55]C. E. Moore, *Atomic Energy Levels*, National Bureau of Standards Circular No. 467 (U. S. Government Printing Office, Washington, D.C., 1949), Vol. 1.
[56]I. Russier-Antoine, A. J. Ross, M. Aubert-Frécon, F. Martin, and P. Crozet, J. Phys. B **33**, 2753 (2000).
[57]R. D. Miles, A. D. Wilkins, L. Morgus, D. O. Kashinski, J. Huennekens, and A. P. Hickman (unpublished).
[58]C. H. Townes and A. L. Schawlow, *Microwave Spectroscopy* (McGraw-Hill, New York, 1955).
[59]H. Katô, Bull. Chem. Soc. Jpn. **66**, 3203 (1993).
[60]K. Ishikawa, J. Chem. Phys. **98**, 1916 (1993).
[61]J. Tellinghuisen, G. Pichler, W. L. Snow, M. E. Hillard, and R. J. Exton, Chem. Phys. **50**, 313 (1980).
[62]R. J. LeRoy and G. T. Kraemer, BCONT 2.1: A Computer Program for Calculating Bound→Continuum Transition Intensities for Diatomic Molecules, Chemical Physics Research Report No. CP-650R, University of Waterloo, 2002.
[63]K. Ishikawa, N. Mukai, and M. Tanimura, J. Chem. Phys. **101**, 876 (1994).
[64]R. Ferber, E. A. Pazyuk, A. V. Stolyarov, A. Zaitsevskii, P. Kowalczyk, H. Chen, H. Wang, and W. C. Stwalley, J. Chem. Phys. **112**, 5740 (2000).
[65]A. J. Ross, C. Effantin, J. d'Incan, and R. F. Barrow, J. Phys. B **19**, 1449 (1986).
[66]P. R. Bevington, *Data Reduction and Error Analysis for the Physical Sciences* (McGraw-Hill, New York, 1969).
[67]L. Morgus, Ph.D. thesis, Lehigh University (unpublished).